High-Performance NiS$_2$ Hollow Nanosphere Cathodes in Magnesium-Ion Batteries Enabled by Tunable Redox Chemistry

Jianbiao Wang,[a] Albertus D. Handoko,[a] Yang Bai,[a] Gaoliang Yang,[a] Yuanjian Li,[a] Zhenxiang Xing,[a] Man-Fai Ng,[b] Zhi Wei Seh[a]*

[a] Institute of Materials Research and Engineering, Agency for Science, Technology and Research (A*STAR), 2 Fusionopolis Way, Innovis, 138634, Singapore.

[b] Institute of High Performance Computing, Agency for Science, Technology and Research (A*STAR), 1 Fusionopolis Way, Connexis, 138632, Singapore.

*Author to whom correspondence should be addressed: sehzw@imre.a-star.edu.sg

ABSTRACT

Two-dimensional metal dichalcogenides have demonstrated outstanding potential as cathodes for magnesium-ion batteries. However, the limited capacity, poor cycling stability and severe electrode pulverization, resulting from lack of void space for expansion, impede their further development. In this work, we report for the first time, nickel sulfide (NiS$_2$) hollow nanospheres assembled with nanoparticles for use as cathode materials in magnesium-ion batteries. Notably,

the nanospheres were prepared by a one-step solvothermal process in the absence of an additive. The results show that regulating the synergistic effect between the rich anions and hollow structure positively affects its electrochemical performance. Crystallographic and microstructural characterizations reveal the reversible anionic redox of $S^{2-}/(S_2)^{2-}$, consistent with density functional theory results. Consequently, the optimized cathode (8-NiS_2 hollow nanospheres) could deliver a large capacity of 301 mA h g^{-1} after 100 cycles at 50 mA g^{-1}, supporting the promising practical application of NiS_2 hollow nanospheres in magnesium-ion batteries.

KEYWORDS: NiS_2, hollow structure, redox chemistry, cathodes, magnesium-ion batteries

Increasing demand for lithium-ion batteries (LIBs), spurred by the rapid adoption of electric vehicles, has exposed significant shortcomings of LIBs, which include safety concerns and lithium supply chain issues.[1-3] The development of safer alternative metal-ion batteries with higher material abundance, higher energy density and longer cycling stability can alleviate such shortcomings.[4-7] A potential alternative to LIBs are rechargeable magnesium-ion batteries (MIBs), which stand out due to their relatively low cost, safety at ambient temperatures, high volumetric capacity (Mg: 3837 mA h cm^{-3}, vs. Li: 2062 mA h cm^{-3}, Na: 1136 mA h cm^{-3}), and suitable reduction potential (-2.4 V vs. standard hydrogen electrode).[8-12] However, industrial adoption of MIBs is impeded by the sluggish electrochemical kinetics of Mg^{2+} caused by electrostatic force and the incompatibility between the electrolyte and electrode.[13-19]

The electrochemical kinetics of Mg^{2+} can be improved by using electrodes made with 2D transition metal dichalcogenides (TMDs) due to their intrinsically high ionic conductivity and the weak interactions between Mg^{2+} and less electronegative host anions.[20-23] Furthermore, TMDs are superior compared to other compounds such as metal oxides as an electrode material because of their unique layered structure and large interlayer spacing, which facilitate the transport of Mg^{2+}.[24-27] Nevertheless, TMD-based electrodes still have significant problems that need to be adequately addressed, including reduced ion mobility and poor rate performance stemming from the high charge density of Mg^{2+}, as well as significant volumetric changes resulting from Mg^{2+} insertion and extraction.[25, 28, 29]

Various strategies have been employed to alleviate these problems, including coupling with carbon-based materials, fabricating microstructures, and introducing heteroatom doping.[30-32]

Notable examples include NiS nanoparticles embedded in carbon nanofibers with a capacity of 265 mA h g^{-1} after 45 cycles at 50 mA g^{-1},[33] CuSe nanoflakes with a capacity of 180 mA h g^{-1} after 100 cycles at 200 mA g^{-1} (218 mA h g^{-1} at 50 mA g^{-1}, rate capacity),[34] and NiS$_2$ nanoparticles in carbon nanotubes, delivering a capacity of 95.2 mA h g^{-1} after 2000 cycles at 200 mA g^{-1} (244.5 mA h g^{-1} at 50 mA h g^{-1}, rate capacity).[30] However, these non-hollow TMD nanostructures are unable to accommodate the large volumetric changes that occur during repeated magnesiation and demagnesiation, resulting in electrode pulverization and poor cycling stability. Therefore, exploring and developing promising cathodes with internal void space and high magnesium storage performance is imperative.

To this end, we developed a one-step solvothermal process to fabricate anion-rich NiS$_2$ hollow nanospheres composed of nanoparticles as a cathode material for MIBs. Hollow NiS$_2$ nanostructures have not been demonstrated as cathodes for MIBs to the best of our knowledge. Our findings reveal that hollow structure rich in anions improved magnesium storage performance. Specifically, the extensive anionic redox in NiS$_2$ contributed to large capacity and long cycling stability. The resulting optimized cathode (8-NiS$_2$) could deliver a capacity of 301 mA h g^{-1} at 50 mA g^{-1} after 100 cycles. Meanwhile, the crystallographic and microstructural characterizations reveal that NiS$_2$ could be reformed during the charging process. The novel design strategy for NiS$_2$ hollow nanospheres could also provide new inspiration for discovering other high-performance TMDs-based cathode materials.

Results and discussion

The NiS_2 hollow nanospheres were prepared via a one-step solvothermal method in the absence of additives (Figure 1a). It is worth noting that the formation of a hollow structure typically requires additives or templates. In this work, the organic nickel compound, nickel(II) acetylacetonate $(Ni(ac)_2)$ and thioacetamide (TAA) were separated as nickel and sulfide sources to obtain the hollow spherical structure via Ostwald ripening.[35] Samples of 4-NiS_2, 6-NiS_2, and 8-NiS_2 hollow nanospheres represent the different ratios of Ni/S that were used in the synthesis (namely, 1:4, 1:6, and 1:8 respectively). The crystal structure of these samples was examined using X-ray diffraction (XRD) (Figure 1b), with the peaks agreeing well with the standard pattern of NiS_2 (JCPDS: 03-065-3325), indicating successful preparation of NiS_2 samples. Well-defined and sharper reflections of NiS_2 were observed with increasing amounts of S loading (8-NiS_2 > 6-NiS_2 > 4-NiS_2), indicating that higher S loading may have increased NiS_2 crystallinity.

X-ray photoelectron spectroscopy (XPS) was further employed to analyze the surface elements of as-prepared samples. The survey spectra (Figure S1) show the apparent co-existence of Ni and S elements. In the high-resolution Ni 2p spectra (Figure 1c), the binding energies at 871.2 and 853.7 eV are assigned to Ni $2p_{1/2}$ and Ni $2p_{3/2}$ of Ni^{2+}, respectively.[36] The peaks for 6-NiS_2 and 4-NiS_2 hollow nanospheres have higher binding energies, indicating the anionic-rich feature of 8-NiS_2 hollow nanospheres.[5, 37] In terms of S 2p spectra (Figure 1d), the binding energies of 8-NiS_2 hollow nanospheres present at 161.7 and 162.8 eV are associated with $(S_2)^{2-}$, and the peaks at 163.8 and 163.9 eV are related to the existence of $(S_n)^{2-}$.[38-40] In comparison, the corresponding peaks of S 2p in 4-NiS_2 and 6-NiS_2 hollow nanospheres have been shifted to higher binding energies, corresponding with the trend seen on Ni 2p. To detect the anionic distribution in NiS_2 hollow

nanospheres, XPS of Ni 2p was conducted with different etching times of 0, 120, 300, and 600 s. For 4-NiS$_2$ and 6-NiS$_2$, a more noticeable shift in Ni 2p XPS spectra was observed with increasing etching time compared to 8-NiS$_2$ (Figure 1e-g). These results demonstrate that the S vacancies existed in the exterior of 4-NiS$_2$ and 6-NiS$_2$. In contrast, no significant XPS shift on 8-NiS$_2$ hollow nanospheres at different etching times confirmed the high content of anions in the exterior and interior of these samples. The abundance of $(S_2)^{2-}$ in 8-NiS$_2$ hollow nanospheres is favorable for redox reactions in the electrochemical process, thus enhancing electrochemical performance.
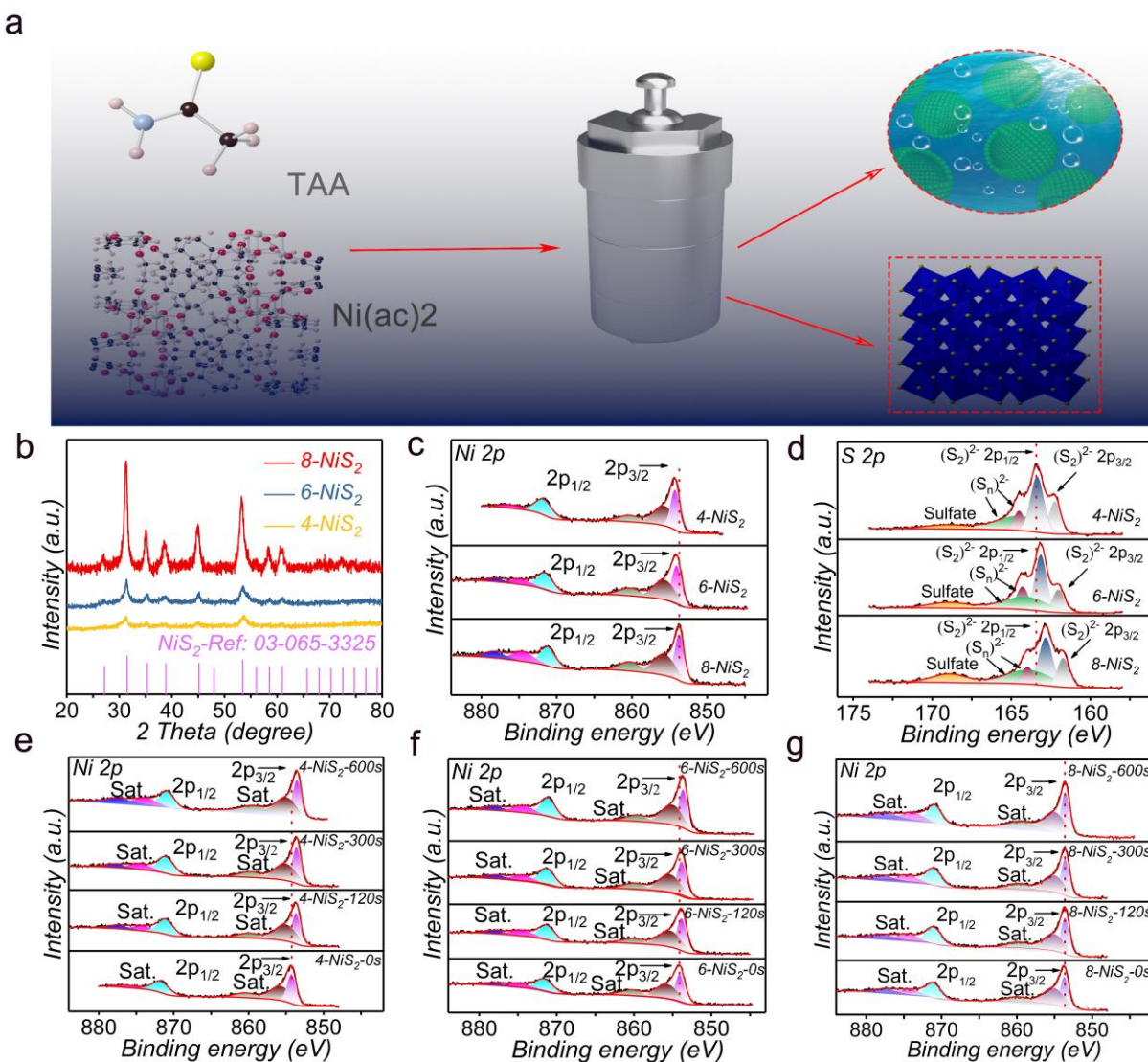
Figure 1. (a) Schematic illustration of the synthesis of NiS_2 hollow nanospheres, (b) XRD patterns, high-resolution XPS spectra of (c) Ni 2p and (d) S 2p, XPS spectra of Ni 2p for (e) 4-NiS_2, (f) 6-NiS_2, and (g) 8-NiS_2 hollow nanospheres, respectively.
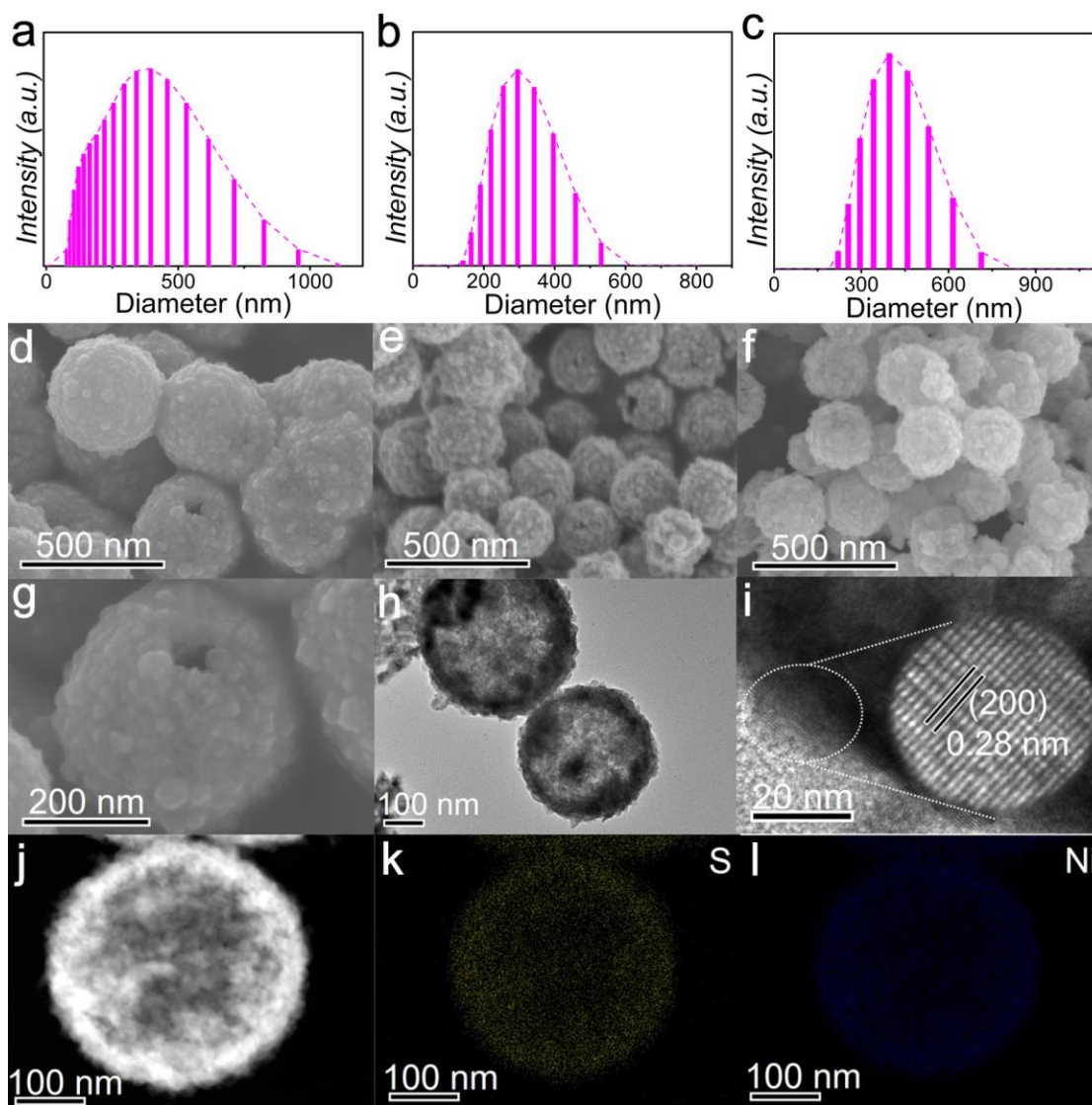

Figure 2. (a-c) Histogram of NiS_2 size distributions for 8-NiS_2, 6-NiS_2, and 4-NiS_2 hollow nanospheres. SEM images of (d) 8-NiS_2, (e) 6-NiS_2, and (f) 4-NiS_2 hollow nanospheres, respectively. (g) SEM image, (h) TEM image, (i) HRTEM image, (j) STEM image, and corresponding EDS mapping of (k) S and (l) Ni in 8-NiS_2 hollow nanospheres.

SEM and TEM images were collected for insight into the morphology and interior structure of NiS_2 hollow nanospheres. The samples of 8-NiS_2, 6-NiS_2, and 4-NiS_2 hollow nanospheres all

possess a spherical morphology (Figure 2(d-f)). The SEM image of 8-NiS$_2$ at higher magnification shows that NiS$_2$ hollow nanospheres consisted of nanoparticles with a diameter of about 250 nm (Figure 2g). A histogram of NiS$_2$ hollow nanospheres size distributions in Figure 2(a-c) show average sizes of 267, 330, and 494 nm for the 8-NiS$_2$, 6-NiS$_2$, and 4-NiS$_2$ hollow nanospheres, respectively. The hollow interior structure can be inferred from the imperfection on the nanospheres, which is corroborated by TEM on the 8-NiS$_2$ sample (Figure 2h). The diameter of the interior structure is estimated to be 180 nm, which could provide sufficient space to accommodate volume variation in the magnesiation/demagnesiation process. For 4-NiS$_2$ and 6-NiS$_2$ hollow nanospheres, the features of the hollow structure have also been observed, as exhibited in Figure S2. The lattice fringe is measured to be 0.28 nm, corresponding to the (200) *d*-spacing, and suggests the successful preparation of 8-NiS$_2$ hollow nanospheres (Figure 2i). mapping images obtained using scanning transmission electron microscopy (STEM) indicate the uniform distribution of Ni and S elements in 8-NiS$_2$ hollow nanospheres (Figure 2(j-l)).

The solvothermal processes are also conducted with different reaction times to support the Ostwald ripening formation mechanism of the hollow structure. Figure S3 shows XRD patterns with varying reaction times of 3 and 12 h (labeled as NiS$_2$-3h and NiS$_2$-12h). The intensity of peaks increased with increasing reaction time, suggesting that the crystalline structure of NiS$_2$ hollow nanospheres is enhanced with the ongoing reaction time. The SEM images (Figure S4) corroborate the XRD findings, where only NiS$_2$-12h hollow nanospheres are composed of well-defined particles compared to NiS$_2$-6h and NiS$_2$-3h. Besides, the SEM images of the samples with reaction times of 10 and 20 min display the presence of particles, while no spherical morphology is found (Figure S5). The microspherical morphology appeared when the reaction time increased to 1 h.

TEM images of samples with different reaction times (1, 3, 6, and 12 h) present the gradual formation of the hollow interior structure from the early solid sphere (Figure S6). These observation results consolidate the Ostwald ripening formation mechanism, in which the particle formed first, then aggregated to form the hollow spherical structure.

The electrochemical properties of NiS_2 hollow nanospheres are evaluated to highlight the importance of anion-rich content in cathode materials. The cycling performance of 4-NiS_2, 6-NiS_2, and 8-NiS_2 hollow nanospheres are tested at a current density of 50 mA g^{-1} (Figure 3a). The electrode of 8-NiS_2 hollow nanospheres delivers a stable capacity of 301 mA h g^{-1} after 100 cycles. For comparison, the electrode of 4-NiS_2 and 6-NiS_2 hollow nanospheres exhibit lower capacity of 220 and 214 mA h g^{-1} after 50 cycles, respectively, suggesting the advantages of anion-rich 8-NiS_2 hollow nanospheres. The intensity of dQ/dV peaks for 8-NiS_2 is also the highest compared with 6-NiS_2 and 4-NiS_2 hollow nanospheres (Figure S7), indicating that the anion-rich NiS_2 is more favorable for the electrochemical process (Figure 3b). The related charge-discharge curves of 8-NiS_2 hollow nanospheres after the 40th, 80th, and 100th cycles share almost overlapping profiles (Figure 3c), indicating the stability of the electrochemical process. Specifically, a stable working voltage above 1.0 V reflects energy density enhancement. As demonstrated in Figure 3d, rate performance has been explored at various current densities of 50–500 mA g^{-1}. For 8-NiS_2 hollow nanospheres, an average capacity of 419.7, 271.8, 135.4, 64.2, and 22.1 mA h g^{-1} can be maintained at the corresponding current densities of 50, 100, 200, 300 and 500 mA g^{-1}, respectively. When the current density returns to 50 mA g^{-1}, a capacity of 466.2 mA h g^{-1} is retained, demonstrating excellent rate capacity reversibility. In contrast, 6-NiS_2 and 4-NiS_2 hollow nanospheres demonstrate poor rate performance and low capacity. The charge-discharge curves of 8-NiS_2 hollow nanospheres at different current densities show that a stable working voltage could be

observed at increasing current densities (Figure 3e). In contrast, the plateaus of 4-NiS$_2$ and 6-NiS$_2$ hollow nanospheres disappear with increasing current densities, highlighting the advantages of anion-rich 8-NiS$_2$ hollow nanospheres (Figure S8).

To explore the diffusion coefficient of Mg^{2+} during the discharge process, the galvanostatic intermittent titration technique (GITT) of the three electrodes was conducted at 50 mA g^{-1} (Figure 3f). The Mg^{2+} diffusion coefficient for 4-NiS$_2$, 6-NiS$_2$, and 8-NiS$_2$ hollow nanospheres are evaluated according to the equation:

$$D_s = \frac{4}{\pi\tau}\left(\frac{n_m V_m}{s}\right)^2 (\frac{\Delta E_s}{\Delta E_t})^2 \tag{1}$$

in which ΔE_s and ΔE_t represent the steady-voltage variation after relaxation and transient voltage change after the discharge process. τ is the relaxation time and V_m is the volume of NiS$_2$ hollow nanospheres. We observed that the Mg^{2+} diffusion coefficient of 8-NiS$_2$ hollow nanospheres calculated from GITT curves is higher than that of 6-NiS$_2$ and 4-NiS$_2$ (Figure 3g). This result indicates that the electrode consisting of 8-NiS$_2$ hollow nanospheres possesses the fastest diffusion coefficient of Mg^{2+}, which account for the superior electrochemical properties of 8-NiS$_2$ hollow nanospheres.

The CV curves at increasing scan rates are presented in Figure S9 to detect the capacity contribution from the diffusion-controlled process and capacitance. The specific contribution was computed based on the following equation:

$$i = k_1 v + k_2 v^{1/2} \tag{2}$$

in which k_1 and k_2 are constants, and v is the sweep rate. It can be observed that capacitance contribution increased with an increase in sweep rates. Specifically, the percentage from capacitance contribution can reach 83.8% at 1 mV s^{-1}, which supports the large capacity and a stable electrochemical performance. The electrochemical impedance spectroscopy (EIS) results suggest that 8-NiS$_2$ hollow nanospheres have a lower resistance after ten cycles than before cycling (Figure S10), explaining the increase in capacity upon cycling. As illustrated in Table S1, the electrode of 8-NiS$_2$ hollow nanospheres demonstrate obvious advantages in terms of capacity and cycles, indicating the successful rational design of the electrodes.[30, 33, 34, 41-46]

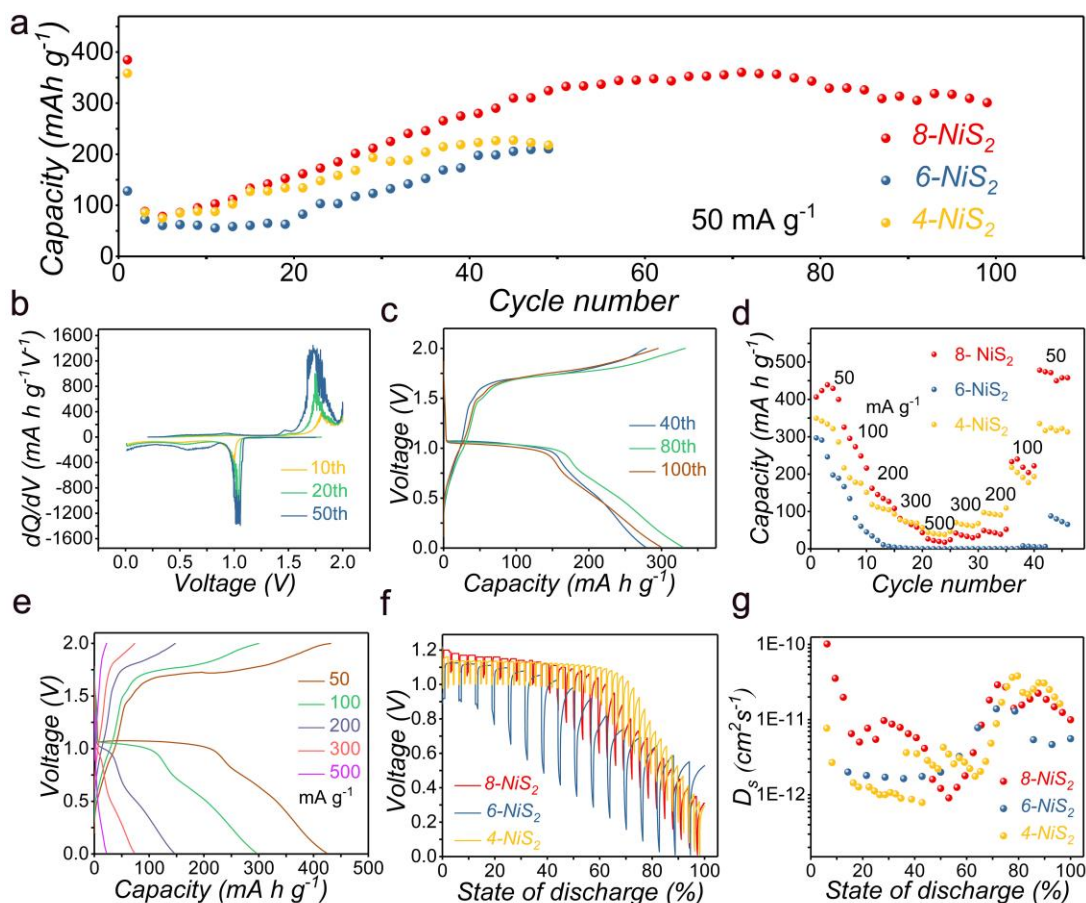

Figure 3. Electrochemical performance of NiS$_2$ hollow nanospheres: (a) cycling performance of 4-NiS$_2$, 6-NiS$_2$, and 8-NiS$_2$ hollow nanospheres at 50 mA g^{-1}, (b) dQ/dV curves, and (c) charge-discharge profiles of 8-NiS$_2$ hollow nanospheres at 50 mA g^{-1}, (d) rate performance, (e) charge-discharge profiles, (f) GITT

curves in the discharge process, and (g) the calculated Mg-ion diffusion coefficient of 4-NiS$_2$, 6-NiS$_2$, and 8-NiS$_2$ hollow nanospheres.
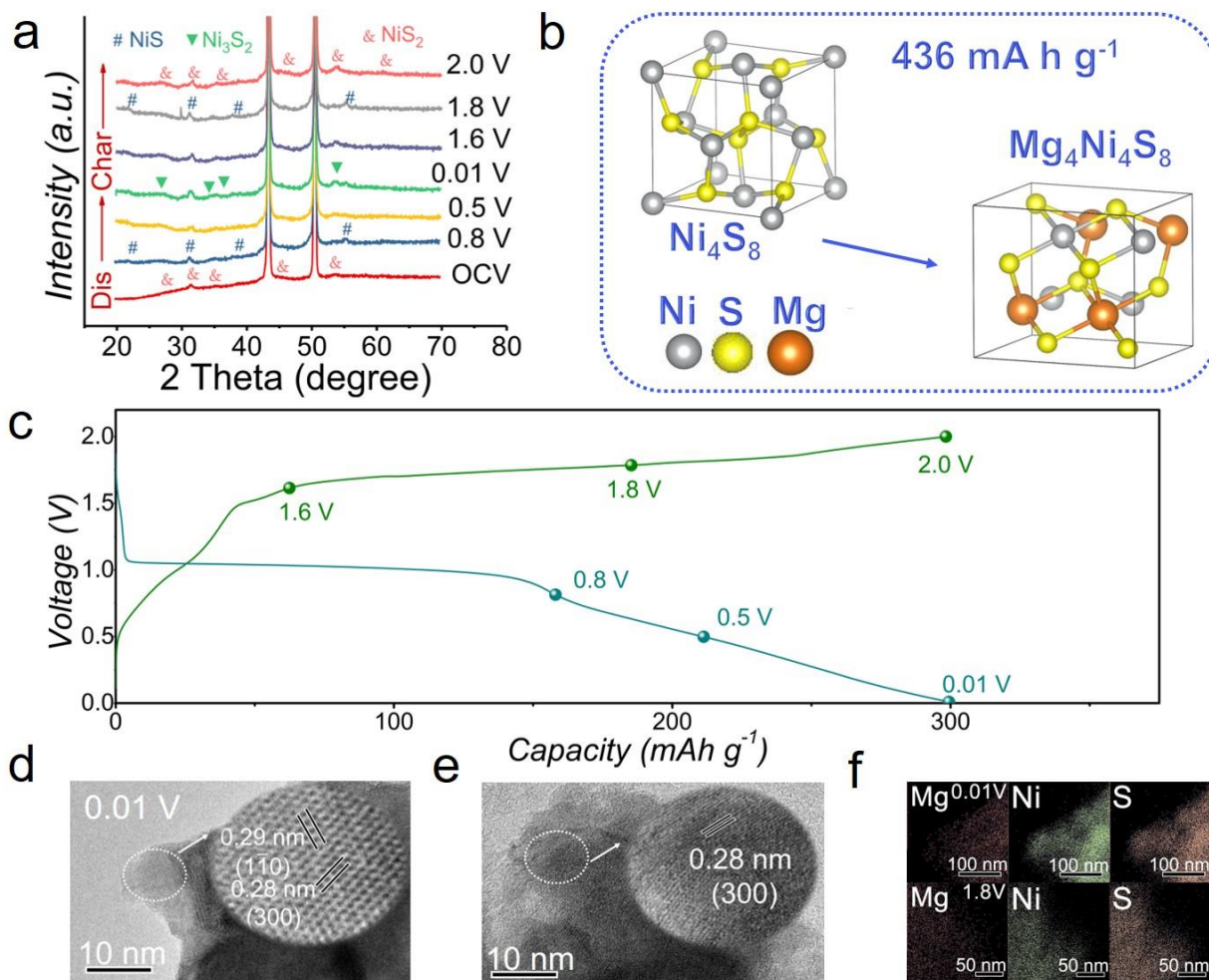

Figure 4. (a) Ex-situ XRD patterns of 8-NiS$_2$ hollow nanospheres at different electrochemical states, (b) schematic of the DFT results, and (c) the corresponding charge-discharge profiles at 50 mA g^{-1}. Ex-situ TEM images of 8-NiS$_2$ hollow nanospheres (d) discharge to 0.01 V, (e) charge to 1.8 V, and (f) the corresponding EDS mapping of 8-NiS$_2$ hollow nanospheres at different potentials.

To systematically understand the working mechanism of 8-NiS$_2$ hollow nanospheres, ex-situ XRD

was performed during the insertion/extraction of Mg^{2+} at different stages of the discharge/charge

process (Figure 4a). When the cell discharged to 0.8 V, the peaks for NiS were observed (JCPDS

no. 001-1286). After discharge to 0.01 V, some new peaks appeared, which could be ascribed to the crystal phase of Ni_3S_2 (JCPDS no. 01-073-0698). During the charging process, peaks of NiS_2 were observed while those of NiS disappeared, clearly indicating a reversible electrochemical process. To provide evidence for the anionic redox reactions $((S_2)^{2-}/S^{2-})$, a selected area of Mg anode was investigated after the discharge process with time-of-flight secondary ion mass spectrometry (TOF-SIMS). The depth profiles and relevant 3D reconstruction of the sputtered volume of several secondary ion fragments of S^- and NiS^- show that the surface of Mg foil has traces of S anions. This should be assigned to some soluble S intermediates, corroborating the anionic redox mechanism (Figure S(11,12)).

From the results of density functional theory (DFT), the $Mg_4Ni_4S_8$ structure is found to be the most favorable in terms of its formation over other numbers of Mg inserted based on insertion energy. The theoretical capacity of this structure is calculated to be 436 mA h g^{-1}, agreeing well with the experimental result. In addition, this magnesiated structure is relatively stable. For example, the crystal structure remains intact when Mg is removed (Figure 4b). The DFT results correlate well with the reversible electrochemical process. The relevant charge-discharge profiles are depicted in Figure 4c, and several electrochemical states are selected for ex-situ characterization. In the discharged state at 0.01 V, the lattice fringes are measured to be 0.28 and 0.29 nm, matching well with (300) and ($1\bar{1}0$) crystal faces of NiS and Ni_3S_2, respectively (Figure 4d). In the charged state at 1.8 V, the primary (300) crystal face of NiS was detected, corresponding with the ex-situ XRD results (Figure 4e). Furthermore, the related EDS mappings show the even distribution of Mg, Ni, and S elements, corresponding with the observation from TEM (Figure 4f). The whole electrochemical process can be summarized as follows:
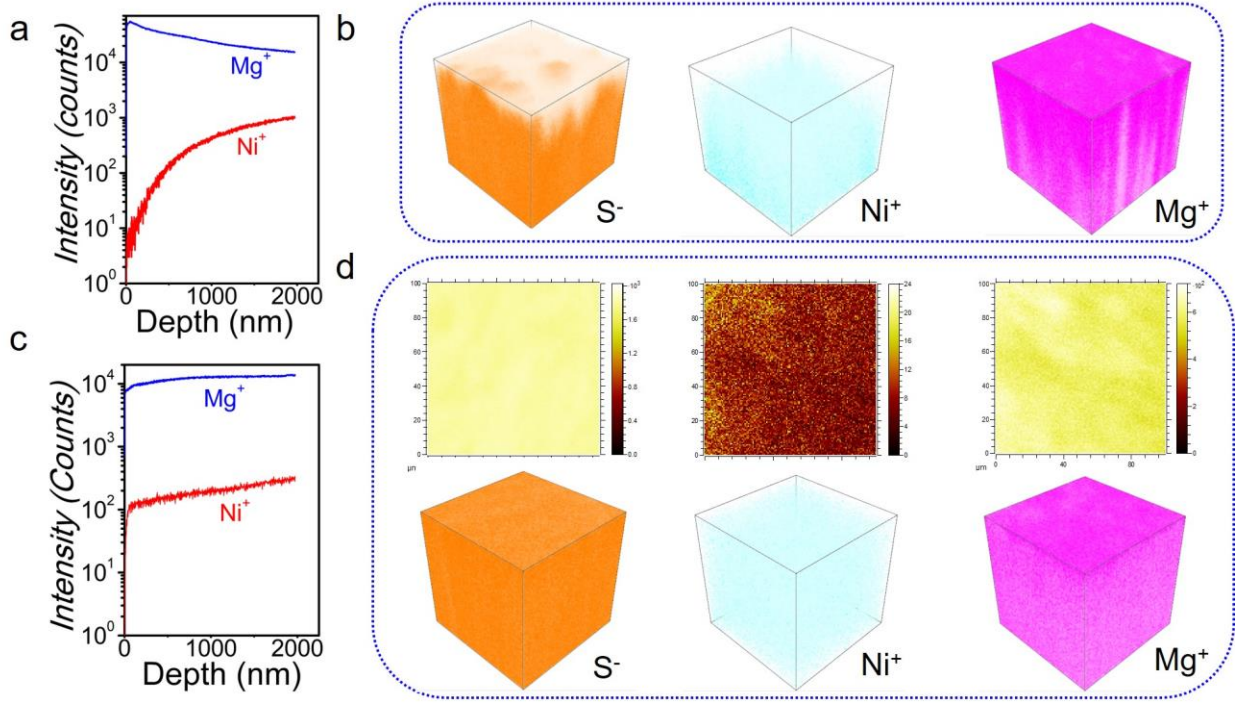
$$NiS_2 + Mg^{2+} + 2e^- \rightarrow NiS + MgS \qquad (3)$$

$$3NiS + Mg^{2+} + 2e^- \leftrightarrow Ni_3S_2 + MgS \qquad (4)$$

Figure 5. (a, c) TOF-SIMS normalized depth profiling of several typical secondary ion fragments (Mg^+, Ni^+) on the electrodes after 8 and 16 discharge cycles, respectively. (b) 3D reconstruction of the sputtered volume of several secondary ion fragments of S^-, Ni^+, and Mg^+ after 8 discharge cycles. (d) 2D render images of the electrode and related 3D reconstructions of S^-, Ni^+, and Mg^+ after 16 discharge processes.

A quantitative analysis of the different cycles (8 and 16 cycles) of the 8-NiS_2 hollow nanospheres cathode is enabled by TOF-SIMS to further investigate the activation effect in the electrochemical process (Figure 5). Figure 5(a, c) shows that the signal intensity of Mg^+ decreases with increasing sputtering depth after 8 discharge cycles and approaches stability after 16 discharge cycles. It indicates the stepwise magnesiated procedure after discharge, consistent with the increasing capacity with ongoing cycles. In terms of Ni^+, a distinctly enhanced intensity of Ni^+ in Figure 5a confirms the difference in distribution between the internal and external areas. Meanwhile, the 3D reconstruction images are visualized in more detail to demonstrate the magnesiation gradient of

NiS$_2$ electrodes after different discharge cycles of 8 and 16 cycles (Figure 5(b, d)). The relevant TOF-SIMS depth profiles of anions (S$^-$, NiS$^-$, MgS$^-$) depicted in Figure S(13-16) confirm our observations.

In conclusion, we assembled NiS$_2$ hollow nanospheres with nanoparticles via a one-step solvothermal process. An anion-rich interface engineering strategy was proposed, and the anionic-redox mechanism was revealed to enhance magnesium storage performance. The electrode consisting of 8-NiS$_2$ hollow nanospheres exhibited a large reversible capacity of 301 mA h g^{-1} after 100 cycles, which is notable for cathodes in magnesium-ion batteries. The outstanding electrochemical performance was due to the following: 1) the hollow structure allows volume variation and complete contact with electrolytes in the charge/discharge process; 2) the existence of nanoparticles reduces the diffusion pathway of Mg^{2+}; 3) the anion-rich interface engineering provides more anionic redox active sites for improving magnesium storage. This design strategy also provides new insight into fabricating other cathodes for high-performance magnesium-ion batteries in the future.

ASSOCIATED CONTENT

Supporting Information

Additional information includes experimental section (synthesis method, characterization methods, electrochemical measurements, DFT methods), XPS survey spectrum, XRD patterns, SEM images, TEM images, dQ/dV curves, charge-discharge profiles, CV rates, table for

electrochemical performance of cathodes, EIS spectra, TOF-SIMS, 2D and 3D images from TOF-SIMS.

Author Contributions

J. W. and Z. W. S conceived the idea. J. W. performed the experiment and wrote the manuscript. A. D. H and Z. W. S. revised the manuscript. G. Y. and Y. B. conducted the XRD experiments. Y. L. and Z. X. conducted the TOF-SIMS experiments. M.-F. N. performed the DFT calculations.

Notes

The authors declare no competing financial interest.

REFERENCES

(1) Sun, Y.; Lee, H.-W.; Seh, Z. W.; Liu, N.; Sun, J.; Li, Y.; Cui, Y. High-capacity battery cathode prelithiation to offset initial lithium loss. *Nat. Energy* **2016,** *1,* 15008.

(2) Seh, Z. W.; Li, W.; Cha, J. J.; Zheng, G.; Yang, Y.; McDowell, M. T.; Hsu, P. C.; Cui, Y. Sulphur-TiO_2 yolk-shell nanoarchitecture with internal void space for long-cycle lithium-sulphur batteries. *Nat. Commun.* **2013,** *4,* 1331.

(3) Liu, K.; Liu, Y.; Lin, D.; Pei, A.; Cui, Y. Materials for lithium-ion battery safety. *Sci. Adv.* **2018,** *4,* 9820.

(4) Zhong, Y.; Xu, X.; Liu, P.; Ran, R.; Jiang, S. P.; Wu, H.; Shao, Z. A Function-Separated Design of Electrode for Realizing High-Performance Hybrid Zinc Battery. *Adv. Energy Mater.* **2020,** *10,* 2002992.

(5) Wang, J.; Huang, J.; Huang, S.; Notohara, H.; Urita, K.; Moriguchi, I.; Wei, M. Rational Design of Hierarchical SnS_2 Microspheres with S Vacancy for Enhanced Sodium Storage Performance. *ACS Sustain. Chem. & Eng.* **2020,** *8,* 9519-9525.

(6) Faegh, E.; Ng, B.; Hayman, D.; Mustain, W. E. Practical assessment of the performance of aluminium battery technologies. *Nat. Energy* **2020,** *6,* 21-29.

(7) Eng, A. Y. S.; Soni, C. B.; Lum, Y.; Khoo, E.; Yao, Z.; Vineeth, S.; Kumar, V.; Lu, J.; Johnson, C. S.; Wolverton, C. Theory-guided experimental design in battery materials research. *Sci. Adv.* **2022,** *8,* 2422.

(8) Regulacio, M. D.; Nguyen, D. T.; Horia, R.; Seh, Z. W. Designing Nanostructured Metal Chalcogenides as Cathode Materials for Rechargeable Magnesium Batteries. *Small* **2021,** *17,* 2007683.

(9) Fu, Q.; Sarapulova, A.; Trouillet, V.; Zhu, L.; Fauth, F.; Mangold, S.; Welter, E.; Indris, S.; Knapp, M.; Dsoke, S.; Bramnik, N.; Ehrenberg, H. In Operando Synchrotron Diffraction and in Operando X-ray Absorption Spectroscopy Investigations of Orthorhombic V_2O_5 Nanowires as Cathode Materials for Mg-Ion Batteries. *J. Am. Chem. Soc.* **2019,** *141,* 2305-2315.

(10) Mao, M.; Gao, T.; Hou, S.; Wang, C. A critical review of cathodes for rechargeable Mg batteries. *Chem. Soc. Rev.* **2018,** *47,* 8804-8841.

(11) Li, Y.; Yang, G.; Sun, S.; Zhang, C.; Lim, C. Y. J.; Wong, A. J. Y.; Lieu, W. Y.; Sofer, Z.; Ng, M. F.; Liu, W.; Seh, Z. W. High Utilization of Composite Magnesium Metal Anodes Enabled by a Magnesiophilic Coating. *Nano Lett.* **2022,** *22,* 6808-6815.

(12) Luo, J.; Bi, Y.; Zhang, L.; Zhang, X.; Liu, T. L. A Stable, Non-Corrosive Perfluorinated Pinacolatoborate Mg Electrolyte for Rechargeable Mg Batteries. *Angew. Chem. Int. Ed.* **2019,** *58,* 6967-6971.

(13) Wang, P.; Buchmeiser, M. R. Rechargeable Magnesium–Sulfur Battery Technology: State of the Art and Key Challenges. *Adv. Funct. Mater.* **2019,** *29,* 1905248.

(14) Davidson, R.; Verma, A.; Santos, D.; Hao, F.; Fincher, C.; Xiang, S.; Van Buskirk, J.; Xie, K.; Pharr, M.; Mukherjee, P. P.; Banerjee, S. Formation of Magnesium Dendrites during Electrodeposition. *ACS Energy Lett.* **2018,** *4,* 375-376.

(15) Eaves-Rathert, J.; Moyer, K.; Zohair, M.; Pint, C. L. Kinetic- versus Diffusion-Driven Three-Dimensional Growth in Magnesium Metal Battery Anodes. *Joule* **2020,** *4,* 1324-1336.

(16) Tchitchekova, D. S.; Ponrouch, A.; Verrelli, R.; Broux, T.; Frontera, C.; Sorrentino, A.; Bardé, F.; Biskup, N.; Arroyo-de Dompablo, M. E.; Palacín, M. R. Electrochemical Intercalation of Calcium and Magnesium in TiS_2: Fundamental Studies Related to Multivalent Battery Applications. *Chem. Mater.* **2018,** *30,* 847-856.

(17) Johnson, I. D.; Ingram, B. J.; Cabana, J. The Quest for Functional Oxide Cathodes for Magnesium Batteries: A Critical Perspective. *ACS Energy Lett.* **2021,** *6,* 1892-1900.

(18) Horia, R.; Nguyen, D. T.; Eng, A. Y. S.; Seh, Z. W. Using a Chloride-Free Magnesium Battery Electrolyte to Form a Robust Anode-Electrolyte Nanointerface. *Nano Lett.* **2021,** *21,* 8220-8228.

(19) Nguyen, D.-T.; Eng, A. Y. S.; Horia, R.; Sofer, Z.; Handoko, A. D.; Ng, M.-F.; Seh, Z. W. Rechargeable magnesium batteries enabled by conventional electrolytes with multifunctional organic chloride additives. *Energy Storage Mater*. **2022,** *45,* 1120-1132.

(20) Liu, F.; Wang, T.; Liu, X.; Fan, L. Z. Challenges and Recent Progress on Key Materials for Rechargeable Magnesium Batteries. *Adv. Energy Mater.* **2021,** *11*, 2000787.

(21) Li, Z.; Mu, X.; Zhao-Karger, Z.; Diemant, T.; Behm, R. J.; Kubel, C.; Fichtner, M. Fast kinetics of multivalent intercalation chemistry enabled by solvated magnesium-ions into self-established metallic layered materials. *Nat. Commun.* **2018,** *9,* 5115.

(22) Zhang, Y.; Cao, J. M.; Yuan, Z.; Xu, H.; Li, D.; Li, Y.; Han, W.; Wang, L. TiVCT$_x$ MXene/Chalcogenide Heterostructure-Based High-Performance Magnesium-Ion Battery as Flexible Integrated Units. *Small* **2022,** *18,* 2202313.

(23) Dey, S.; Lee, J.; Britto, S.; Stratford, J. M.; Keyzer, E. N.; Dunstan, M. T.; Cibin, G.; Cassidy, S. J.; Elgaml, M.; Grey, C. P. Exploring Cation-Anion Redox Processes in One-Dimensional Linear Chain Vanadium Tetrasulfide Rechargeable Magnesium Ion Cathodes. *J. Am. Chem. Soc.* **2020,** *142,* 19588-19601.

(24) Xiong, F.; Fan, Y.; Tan, S.; Zhou, L.; Xu, Y.; Pei, C.; An, Q.; Mai, L. Magnesium storage performance and mechanism of CuS cathode. *Nano Energy* **2018,** *47,* 210-216.

(25) Shen, Y.; Wang, Y.; Miao, Y.; Yang, M.; Zhao, X.; Shen, X. High-Energy Interlayer-Expanded Copper Sulfide Cathode Material in Non-Corrosive Electrolyte for Rechargeable Magnesium Batteries. *Adv. Mater.* **2020,** *32,* 1905524.

(26) Du, A.; Zhao, Y.; Zhang, Z.; Dong, S.; Cui, Z.; Tang, K.; Lu, C.; Han, P.; Zhou, X.; Cui, G. Selenium sulfide cathode with copper foam interlayer for promising magnesium electrochemistry. *Energy Storage Mater.* **2020,** *26,* 23-31.

(27) Wang, J.; Luo, N.; Wu, J.; Huang, S.; Yu, L.; Wei, M. Hierarchical spheres constructed by ultrathin VS_2 nanosheets for sodium-ion batteries. *J. Mater. Chem. A* **2019,** *7,* 3691-3696.

(28) Wang, J.; Okabe, J.; Urita, K.; Moriguchi, I.; Wei, M. Cu_2S hollow spheres as an anode for high-rate sodium storage performance. *J. Electroanal. Chem.* **2020,** *874,* 114523.

(29) Mao, M.; Gao, T.; Hou, S.; Wang, F.; Chen, J.; Wei, Z.; Fan, X.; Ji, X.; Ma, J.; Wang, C. High-Energy-Density Rechargeable Mg Battery Enabled by a Displacement Reaction. *Nano Lett.* **2019,** *19,* 6665-6672.

(30) Ye, Z.; Li, P.; Wei, W.; Huang, C.; Mi, L.; Zhang, J.; Zhang, J. In Situ Anchoring Anion-Rich and Multi-Cavity NiS_2 Nanoparticles on NCNTs for Advanced Magnesium-Ion Batteries. *Adv. Sci.* **2022,** *9,* 2200067.

(31) Xu, H.; Li, Y.; Zhu, D.; Li, Z.; Sun, F.; Zhu, W.; Chen, Y.; Zhang, J.; Ren, L.; Zhang, S.; Zou, J.; Laine, R. M. Synchrotron Radiation Spectroscopic Studies of Mg^{2+} Storage Mechanisms

in High-Performance Rechargeable Magnesium Batteries with Co-Doped FeS_2 Cathodes. *Adv. Energy Mater.* **2022,** *12,* 2201608.

(32) Jing, P.; Lu, H.; Yang, W.; Cao, Y. Interlayer-expanded and binder-free VS_2 nanosheets assemblies for enhanced Mg^{2+} and Li^+/Mg^{2+} hybrid ion storage. *Electrochim. Acta* **2020,** *330,* 135263.

(33) Zhu, G.; Xia, G.; Pan, H.; Yu, X. Size-Controllable Nickel Sulfide Nanoparticles Embedded in Carbon Nanofibers as High-Rate Conversion Cathodes for Hybrid Mg-Based Battery. *Adv. Sci.* **2022,** *9,* 2106107.

(34) Zhang, Y.; Zhu, Y.; Wang, Z.; Peng, H.; Yang, X.; Cao, Y.; Du, C.; Ma, X.; Cao, C. Pulverization-Tolerant CuSe Nanoflakes with High (110) Planar Orientation for High-Performance Magnesium Storage. *Adv. Funct. Mater.* **2021,** *31,* 2104730.

(35) Huo, J.; Wang, L.; Irran, E.; Yu, H.; Gao, J.; Fan, D.; Li, B.; Wang, J.; Ding, W.; Amin, A. M.; Li, C.; Ma, L. Hollow Ferrocenyl Coordination Polymer Microspheres with Micropores in Shells Prepared by Ostwald Ripening. *Angew. Chem. Int. Ed.* **2010,** *49,* 9237-9241.

(36) Li, Y.; Dai, T.; Wu, Q.; Lang, X.; Zhao, L.; Jiang, Q. Design heterostructure of NiS–NiS_2 on NiFe layered double hydroxide with Mo doping for efficient overall water splitting. *Mater. Today Energy* **2022,** *23,* 100906.

(37) Wang, J.; Huang, J.; Huang, S.; Komine, Y.; Notohara, H.; Urita, K.; Moriguchi, I.; Wei, M. Regulating the effects of SnS shrinkage in all-solid-state lithium-ion batteries with excellent electrochemical performance. *Chem. Eng. J.* **2022,** *429,* 132424.

(38) Li, S.; Yang, G.; Ge, P.; Lin, H.; Wang, Q.; Ren, X.; Luo, S.; Philo, D.; Chang, K.; Ye, J. Engineering Heterogeneous NiS_2/NiS Cocatalysts with Progressive Electron Transfer from Planar p-Si Photocathodes for Solar Hydrogen Evolution. *Small methods* **2021,** *5,* 2001018.

(39) Zhao, H.; Li, W.; Wang, R. One-pot synthesis and microstructure analysis of Fe-doped NiS_2 for efficient oxygen evolution electrocatalysis. *Mater. Adv.* **2022,** *3,* 7125-7131.

(40) Li, Y.; Chen, J.; Zhang, Y.; Yu, Z.; Zhang, T.; Ge, W.; Zhang, L. NiS_2/rGO/S capable of lithium polysulfide trapping as an enhanced cathode material for lithium sulfur batteries. J. Alloys Compd. **2018,** *766,* 804-812.

(41) Qu, X.; Du, A.; Wang, T.; Kong, Q.; Chen, G.; Zhang, Z.; Zhao, J.; Liu, X.; Zhou, X.; Dong, S.; Cui, G. Charge-Compensation in a Displacement Mg^{2+} Storage Cathode through Polyselenide-Mediated Anion Redox. *Angew. Chem. Int. Ed.* **2022,** *61,* 202204423.

(42) Du, C.; Zhu, Y.; Wang, Z.; Wang, L.; Younas, W.; Ma, X.; Cao, C. Cuprous Self-Doping Regulated Mesoporous CuS Nanotube Cathode Materials for Rechargeable Magnesium Batteries. *ACS Appl. Mater. Interf.* **2020,** *12,* 35035-35042.

(43) Mao, M.; Tong, Y.; Zhang, Q.; Hu, Y. S.; Li, H.; Huang, X.; Chen, L.; Gu, L.; Suo, L. Joint Cationic and Anionic Redox Chemistry for Advanced Mg Batteries. *Nano Lett.* **2020,** *20,* 6852-6858.

(44) Wu, C.; Zhao, G.; Yu, X.; Liu, C.; Lyu, P.; Maurin, G.; Le, S.; Sun, K.; Zhang, N. MoS_2/graphene heterostructure with facilitated Mg-diffusion kinetics for high-performance rechargeable magnesium batteries. *Chem. Eng. J.* **2021,** *412,* 128736.

(45) Ding, S.; Dai, X.; Li, Z.; Wang, C.; Meng, A.; Wang, L.; Li, G.; Huang, J.; Li, S. PVP-induced synergistic engineering of interlayer, self-doping, active surface and vacancies in VS_4 for enhancing magnesium ions storage and durability. *Energy Storage Mater*. **2022,** *47,* 211-222.

(46) Chen, D.; Du, F.; Cao, S.-a.; Li, T.; Xu, F. $Co_{0.85}Se$ hollow polyhedrons entangled by carbon nanotubes as a high-performance cathode for magnesium secondary batteries. *Chem. Eng. J.* **2022,** *428,* 129545.

Table of Contents (TOC) Graphic